



Experimental and ab-initio investigation of the microstructure and optoelectronic properties of FCM–CVD-prepared Al-doped ZnO thin films

Ilyass Jellal¹ · Hassan Ahmoum² · Yassine Khaissa¹ · Khalid Nouneh¹ · Mourad Bouhrara² · Mounir Fahoume¹ · Siddheshwar Chopra³ · Jamal Naja⁴

Received: 8 March 2019 / Accepted: 24 June 2019 / Published online: 27 August 2019
© Springer-Verlag GmbH Germany, part of Springer Nature 2019

Abstract

In this research, pure and aluminium-doped zinc oxide (ZnO) thin films (5–50%) have been synthesized by the fine-channel mist chemical vapor deposition (FCM-CVD) technique. The microstructure and optoelectronic properties of the films have been characterized with the help of scanning electron microscope (SEM), X-ray diffraction (XRD), and UV–visible absorption (UV–Vis), respectively. The critical-doping (Al) concentration of ZnO was found to be 10%. Below this concentration of Al, the preferential orientation of the films was found to be along (002). Moreover, the films are in tensile states and the optical bandgap values found to be decreasing. For heavy doping concentration, the films are found to be in the compression states, and the optical bandgap increased with the Al concentration. To validate our experimental results, DFT calculations were performed to show and explain the origin of the variation of bandgap, tensile, and compression states.

1 Introduction

Zinc oxide is an abundant material, and has many notable benefits such as diversified morphology, thermodynamic stability, high photosensitivity, low-cost, direct electron transitions, and a large exciton energy (60 meV) [1]. These advantages and characteristics transform it to a material which is widely used in industry for many applications, such as transparent conducting electrode for photovoltaics applications [2], light-emitting diodes [3, 4], phosphorescent and luminescent material in the visible (blue–green) and

ultraviolet regions [5], and also for photocatalytic applications [6]. Zinc oxide has a wide bandgap (3.37 eV) for the most stable structure (Wurtzite) obtained under atmospheric pressure [7]. The application of ZnO for photocatalysis degradation needs UV light sources due to its wide bandgap [8]. Unfortunately, these sources of light may be harmful for humans and expensive at the same time. On the contrary, solar energy is free, clean, renewable, and totally inexhaustible. To take advantage of these benefits, doping ZnO may be necessary to enhance its absorption of the solar spectrum and its performance in view of photocatalytic applications. N-type doping of ZnO is easily achieved by replacing Zn²⁺ ions with group-III metals such as In³⁺, Ga³⁺, or Al³⁺. However, aluminum is the preferred choice due to the advantages such as abundance, inexpensive, nontoxic, and good electrical conductivity [9].

Many different techniques have been used to deposit ZnO thin films, such as successive ionic layer adsorption and reaction (SILAR) [10], RF sputtering [11], co-sputtering [12], hydrothermal synthesis [13, 14], electrodeposition [15], spin-coating [16, 17], spray pyrolysis [18], pulsed laser [19], and mist chemical vapor deposition (Mist-CVD) [20, 21]. The mist chemical vapor deposition is a simple technique for the deposition of thin films, and has several advantages such as: low-cost, environmentally friendly and that it is used under atmospheric pressure. It works by atomizing

✉ Khalid Nouneh
khalid.nouneh@uit.ac.ma

¹ Laboratory of Physics of Condensed Matter (LPMC), Department of Physics, Faculty of Sciences, Ibn Tofail University, BP 133, Kenitra, Morocco

² Materials Physics and Systems Modeling Laboratory (LP2MS), Unit Associated At CNRST-URAC:08, Faculty of Sciences, Moulay Ismail University, BP 11201, Zitoune, Meknes, Morocco

³ Department of Physics, Amity Institute of Applied Sciences, Amity University, Noida, India

⁴ Applied Chemistry and Environment, Faculty of Science and Technology, Hassan 1st University, BP 577, Route de Casablanca, Settat, Morocco

the solution into fine particles (1–10 μm) using an ultrasonic generator. The mist is formed without an initial speed and that is why a carrier gas is needed to transfer it to the deposition area. This technique is a combination of spray pyrolysis and chemical vapor deposition [22], and represents an easy way for doping, by simply adding the impurities to the precursor solution. The mist chemical vapor deposition technique has three different modes of operation: the hot-wall, the linear source nozzle, and the fine channel. Here, we have used the last mode to deposit the ZnO thin films. The fine-channel mist–CVD (FCM–CVD) system has been designed for the source to firmly and effectively be insufflated onto the substrate, enhancing the partial pressure of the source precursor, so that the reaction for the film formation can firmly occur against thermal convection [23].

It has been reported that doping ZnO with Al leads to a reduction in the visible region transmittance and increase in the optical bandgap, which is unfavourable for the solar cell applications. In this study, we have synthesized and characterized aluminum-doped ZnO using FCM–CVD for the first time and we expect that this research will be of benefit to the research community working on the fabrication of solar cell devices based on ZnO:Al and also would enhance their understanding in the photocatalytic applications.

2 Experimental and theoretical details

Undoped and Al-doped ZnO thin films were grown by fine-channel mist chemical vapor deposition (FCM–CVD) technique. First, the solution was atomized into mist droplets using an ultrasonic generator working at 2.4 MHz [24]. The mist particles formed henceforth were then transferred to the reactor with a carrier gas and decomposed on the substrate by heat energy. Finally, the decomposed particles were oxidized to metallic oxide [22]. Figure 1 illustrates the components of the FCM–CVD technique.

Thin films were synthesized onto a glass substrate cleaned in acetone bath for 15 min, followed by the methanol bath for 15 min and finally in distilled water for 15 min. As a starting material, zinc chloride (ZnCl_2) and aluminum chloride hexahydrate ($\text{AlCl}_3 \cdot 6\text{H}_2\text{O}$) were used as a zinc source and dopant source, respectively. Zinc chloride was dissolved in distilled water at room temperature to obtain 0.08 M solution. The deposition was maintained at 450 $^\circ\text{C}$ for 10 min, and an ultrasonic generator operating at 2.4 MHz was used to atomize the solution into mist droplets. The mist formed was transferred into the reaction zone with O_2 gas (carrier gas = 2.5 L/min, diluted gas = 5 L/min). Pure and Al-doped ZnO thin films were grown in the same conditions. The nominal molar concentrations of Al in the precursor solution were fixed at 5%, 10%, 25%, and 50%, respectively.

The structure of synthesized ZnO thin films was observed by an X-ray diffractometer (XRD) (Panalytical Xpert pro, with $\text{CuK}\alpha$ radiation ($\lambda = 1.54 \text{ \AA}$)). UV–Vis transmittance spectra were obtained with the help of a Lambda-35 PerkinElmer spectrometer. The film surface and cluster size of ZnO thin films were analyzed by scanning electron microscopy (SEM) (JEOL JSM-IT100).

Furthermore, all the theoretical calculations were performed with the help of the first-principles pseudopotential scheme based on the density functional theory (DFT) and the plane-wave method [25], respectively. The exchange and correlation effects have been treated under the generalized gradient approximation (GGA) with Perdew–Burke–Ehrenkoff (PBE) functional [26], and the valence electron configuration was treated with the help of ultrasoft Pseudopotential (USP) method, respectively. The kinetic energy and the charge density cutoffs were set at 40 Ry and 400 Ry, respectively. A $4 \times 4 \times 4$ Monkhorst Pack grid was employed for the k-point sampling [27], while the convergence threshold for the self-consistent-field iteration was set at 10^{-7} Ry, respectively. Broyden–Fletcher–Goldfarb–Shanno (BFGS) method was used for the optimization of ion positions until the force on every atom is less than 0.0001 Ry per a.u. respectively.

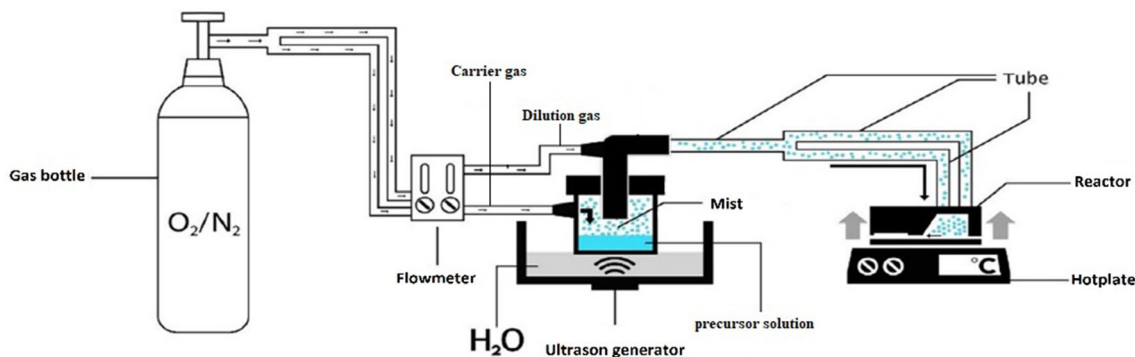


Fig. 1 Components of the FCM–CVD technique used for deposition of undoped and Al-doped ZnO thin films

3 Results and discussion

Figure 2 shows the XRD spectra of ZnO samples doped with different concentrations of aluminum. All the films deposited are found to be polycrystalline in nature with diffraction peaks confirming with DATA pdf card No. 01-070-2551. Moreover, it indicates that the films are crystallized with the Wurtzite structure. However, no diffraction peak related to the secondary phase of Al or Al₂O₃ has been noticed at various concentrations, indicating a high solubility of Al in the ZnO thin films using FCM-CVD, respectively.

Here, the sharp diffraction peaks obtained indicate high crystallinity of the thin films synthesized [28] by the FCM-CVD method. For dopant concentrations below 25%, the peak (002) was the most predominant, indicating that the preferential orientation of the growth was along the *c*-axis. Notably, an increase in the aluminum concentration leads to a change in the preference orientation from (002) to (100) direction. It could be due to an increase in the stress caused by the ion size differences between aluminum and zinc [29]. This result is in agreement with other works [30–32].

The crystallite size (*D*) of the films was calculated using Scherrer formula [33, 34], the lattice parameters (*a* and *c*) were calculated using Bragg’s law for hexagonal system,

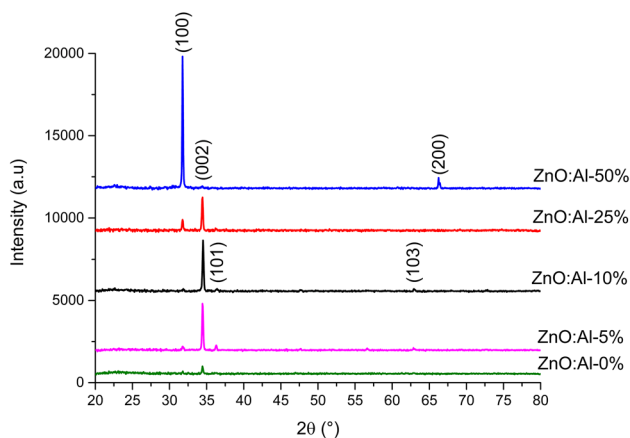


Fig. 2 XRD spectra of undoped and doped ZnO thin films with different aluminum concentrations

the average uniform strain (\mathcal{E}) in the lattice along the *c*-axis were also calculated [35], and the stress (σ) in the plane of the films was calculated using the biaxial strain model [35]. The calculated parameters are listed in Table 1.

The stress in the film could be due to several factors such as the impurities introduced, defect, and lattice distortion in the crystal (intrinsic stress), or by the lattice mismatch and thermal expansion coefficient mismatch between the film and substrate (extrinsic stress). However, the extrinsic stress can be negligible if the thickness of the film is larger [36].

For Al-dopant concentrations ranging from 0 to 10%, stress values were positive, indicating that the films are in the state of tensile-state stress [37]. However, it can be seen that this value increases with the dopant concentration, which is probably due to the incorporation of more Al³⁺ ions in the ZnO host lattice. For high-dopant concentration (25% and 50%), the value of the stress is negative, indicating that the films are in a state of compressive stress [38]. For ZnO doping, it is mentioned that there is a critical value of the aluminum concentration up to which the stress increases, and above this value, the stress decreases. For aluminum concentrations above this critical value, the aluminum atoms are positioned at the interstitial sites instead of being substituted for the zinc atoms [39]. The same result was obtained in another work, in which the stress of the ZnO films was changed from the tensile state to the compressive state due to the increase in aluminum concentration [40].

The SEM micrographs of the surface of the layers are represented in Fig. 3. SEM observations of undoped ZnO and Al-5%-doped ZnO showed that all the surfaces of these films had no structural surface anomalies, and their external morphologies indicate a uniform (homogeneous) distribution of the deposited material. The hexagonal structure of the grains was clearly observed in case of the undoped films, but this structure, however, got affected upon doping. When the dopant concentrations were increased to (10%, 25% and 50%), the creation of more space between the grains was observed, along with a change in the grain forms.

Figure 4 shows the top view of the growth of ZnO-based crystals in different directions [(002), (101), and (100)], respectively. The top view of the crystal growth along the plane (002) shows the appearance of the hexagons (Fig. 4a), the growth along the plane (101) shows the appearance of

Table 1 Structural properties of undoped and Al-doped ZnO thin films with Al different concentrations

| Sample | <i>a</i> (Å) | <i>c</i> (Å) | <i>c/a</i> | \mathcal{E} (10 ⁻⁴) | σ (GPa) | β (°) | <i>D</i> (nm) |
|----------------------|--------------|--------------|------------|-----------------------------------|----------------|-------------|---------------|
| DATA No. 01-070-2551 | 3.249 | 5.207 | 1.602 | – | – | – | – |
| Undoped ZnO | 3.255 | 5.205 | 1.599 | – 3.84 | 0.174 | 0.165 | 50 |
| Al-5% doped ZnO | 3.246 | 5.204 | 1.603 | – 5.76 | 0.261 | 0.181 | 46 |
| Al-10% doped ZnO | 3.237 | 5.196 | 1.605 | – 21.12 | 0.958 | 0.193 | 43 |
| Al-25% doped ZnO | 3.254 | 5.209 | 1.600 | 3.84 | – 0.174 | 0.191 | 44 |
| Al-50% doped ZnO | 3.253 | 5.215 | 1.603 | 15.36 | – 0.697 | 0.147 | 56 |

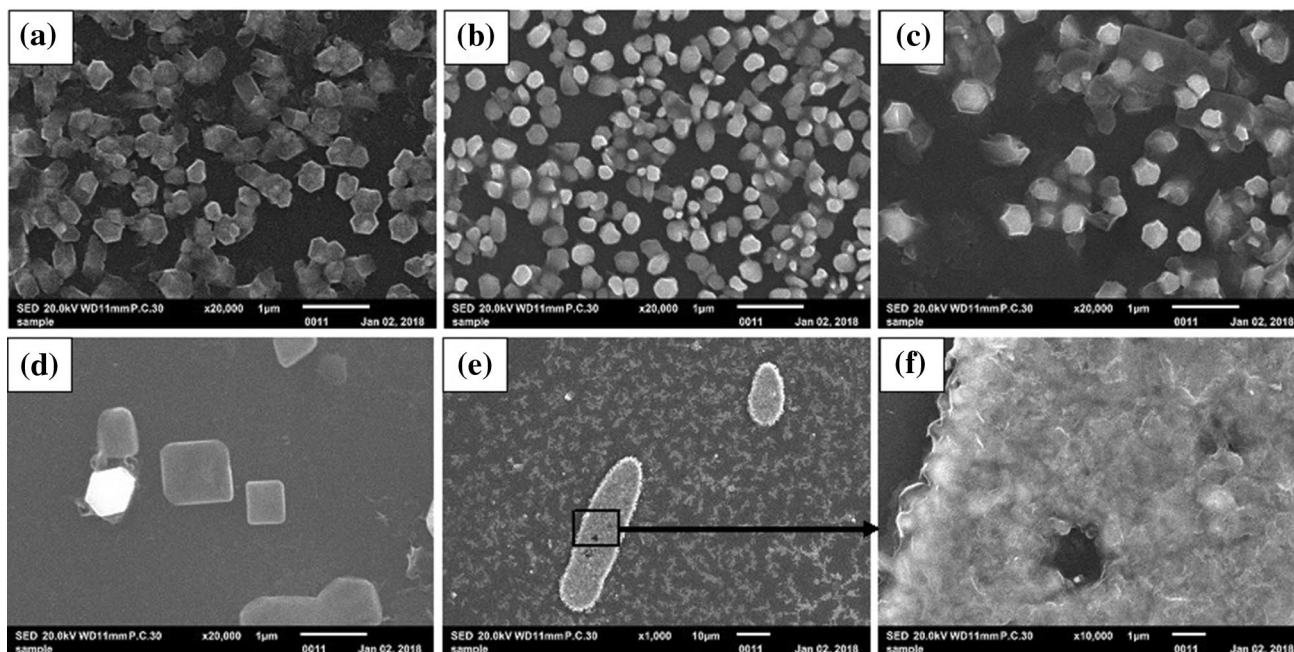


Fig. 3 Surface images of undoped and doped ZnO films, **a** undoped, **b** 5% Al doping, **c** 10% Al doping, **d** 25% Al doping, **e** 50% Al doping, and **f** zoomed-in image of the zone indicated by the black rectangular box depicted in (e)

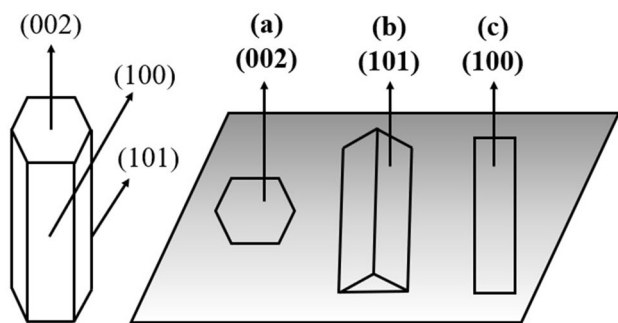


Fig. 4 Orientational crystal growth views of ZnO thin films. **a** Perpendicular to the substrate for a columned structure, **b** parallel to the substrate for a pyramid like structure, and **c** parallel to the substrate for a polygon structure

the pyramids (Fig. 4b), and the growth according to the plane (100) shows the appearance of the polygons (Fig. 4c), respectively. The appearance of polygon structure in the ZnO:Al-25% sample indicates the change in the growth orientation to the (100) plane. This is explained in Fig. 4 and, moreover, also confirmed by the XRD results in Fig. 2.

The transmission spectra of undoped and doped ZnO thin films are shown in Fig. 5. The transmittance decreased with the increasing doping concentrations from 0 to 10%, and this may be due to the increase in the charge density, which results in a higher absorption of the photons reaching the sample [41]. For higher concentrations of the dopant (25% and 50%), the transmittance is found to increase and

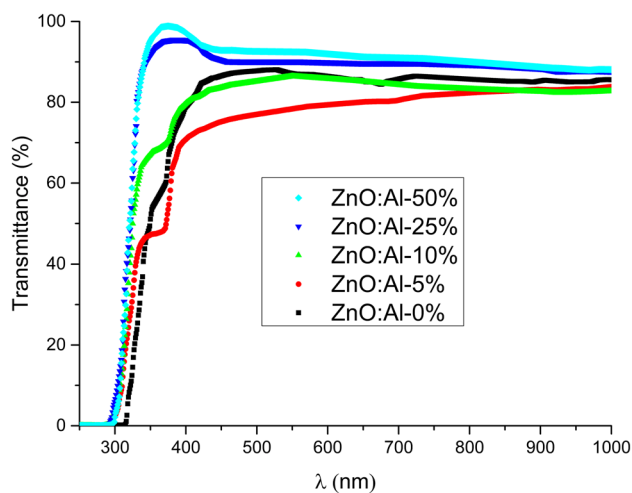


Fig. 5 Optical transmission spectra of undoped and doped ZnO thin films for various Al concentrations

this could be due to an increase in the voids in the sample according to the SEM images.

The determination of the optical bandgap E_g was based on the model proposed by Tauc [42]. The values of E_g obtained were: 3.3 eV, 3.21 eV, 3.25 eV, 3.88 eV, and 3.86 eV for dopant concentrations 0%, 5%, 10%, 25%, and 50%, respectively (see Fig. 6). In case of lower doping concentrations (5% and 10%), the bandgap was found to decrease by the doping process, and this could be attributed to the incorporation of Al^{3+} ions which replace the substitutional or

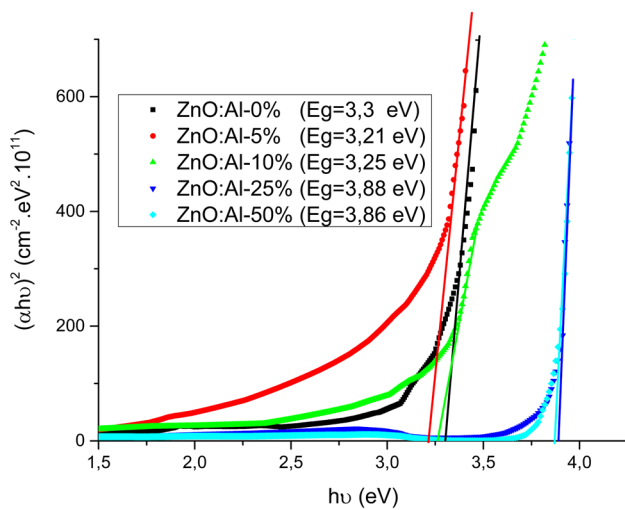


Fig. 6 Optical bandgap calculated from the Tauc formula for undoped and Al-doped ZnO thin films

interstitial Zn^{2+} ions from the host lattice. This results in an increase in the number of free electrons. Moreover, the introduction of impurities (Al^{3+} ions) produces stress in the films, causing the deformation of the crystal or the creation of defects in the ZnO matrix, respectively. Furthermore, this will increase the scattering of light in the defects [43]. At higher dopant concentrations (25% and 50%), three situations are possible, (i) phase segregation of Al from zinc oxide, (ii) formation of spinel $ZnAl_2O_4$ [44], or (iii) creation of a metastable $(ZnO)_3(Al_2O_3)$ phase [45]. The situation (i) and (ii) were excluded by [46], because no secondary phases were observed by the XRD analysis. Therefore, the metastable phase $(ZnO)_3(Al_2O_3)$ is responsible for the change in the XRD spectra and the optical data [45]. It is known that for

ZnO and Al_2O_3 , the ideal bandgap values are 3.27 eV and 8.7 eV, respectively. Therefore, the increase in the bandgap values may be due to the formation of Al_2O_3 compound with the zinc oxide phase [46]. Our results are in agreement with other work [46], where the bandgap value increased from 3.23 to 3.73 eV upon Al doping, with concentration increasing from 0 to 24.6 at%, respectively.

To understand the variation of the bandgap, the electronic structure and partial and total density of states for each doping concentration were calculated by employing the first-principles calculations based on the popular density functional theory (DFT), respectively. Figures 7a and 8a present the effect of Al impurities on the band structure.

In this work, all the materials were found to possess a direct bandgap, which is desirable for the photocatalysis applications. The incorporation of Al in the ZnO material results in shifting of the fermi level into the conduction band, resulting in a deep donor level in the conduction band. This also indicates that the materials are n-type degenerated semiconductors. This behaviour can be explained by the penetration of Al atoms in ZnO films, giving one free electron to the material and resulting an increase of donor concentration and hence the enhancement in the transformation of the material to a n-type degenerate semiconductor.

Table 2 presents the values of the bandgap for undoped and Al-doped ZnO thin films. The bandgap of undoped ZnO film obtained is in excellent accord with the other theoretical investigations: 0.792 eV [47] and 0.809 eV [48]. The calculated values of the bandgap are much smaller compared to the experimental value (3.3 eV). This is attributed to well-known fact that the bandgap is often underestimated by the GGA optimization. However, the analysis about the variation trend of the bandgap remains unaffected by this underestimation [48].

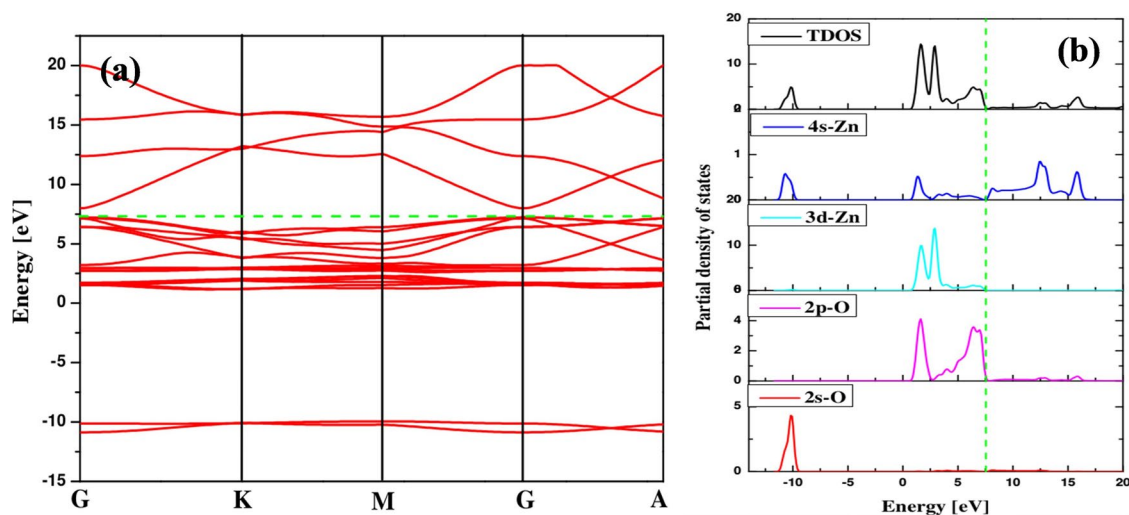


Fig. 7 a Energy-level diagram of undoped ZnO, and b total and partial density of states of undoped ZnO

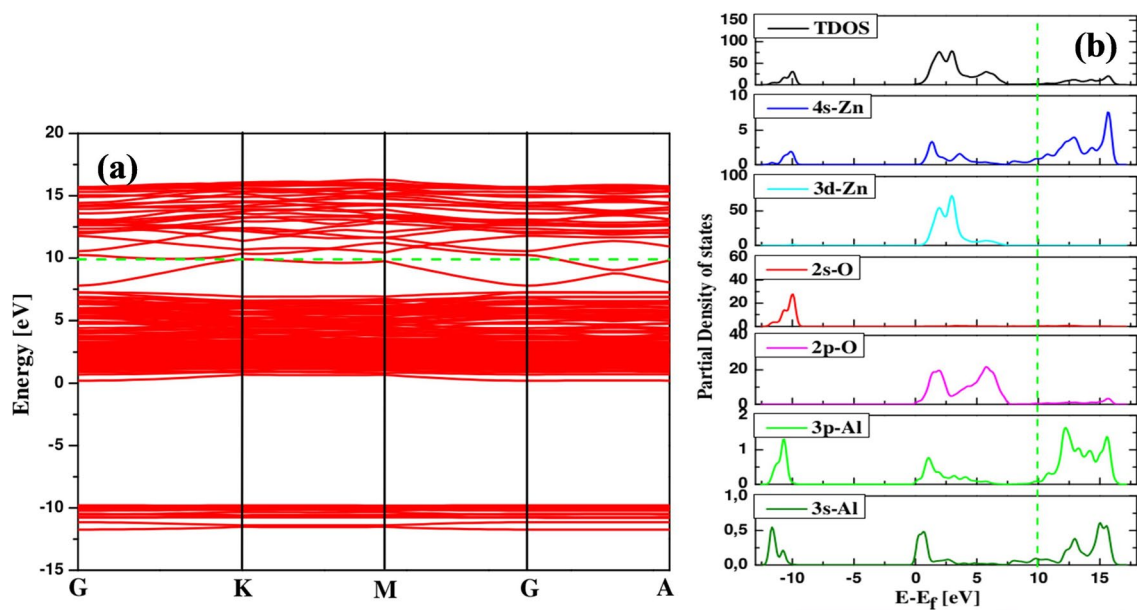


Fig. 8 **a** Band structure of 6.25%-Al-doped ZnO, and **b** total and partial density of states of 6.25%-Al-doped ZnO

Table 2 Theoretical bond length and bandgap of undoped and Al-doped ZnO

| Sample | $d(\text{Zn-O})$ (Å) | $d(\text{Al-O})$ (Å) | E_g (eV) |
|--------------------|----------------------|----------------------|------------|
| Undoped ZnO | 1.986 | – | 0.773 |
| Al-3.14% doped ZnO | 2.056 | 1.783 | 0.696 |
| Al-6.25% doped ZnO | 2.142 | 1.775 | 0.540 |
| Al-14.5% doped ZnO | 2.364 | 1.766 | 0.381 |
| Al-25% doped ZnO | 2.291 | 1.779 | 0.5836 |

As a result, the bandgap decreases with the presence of Al until 14.5% doping concentration, which agrees well with the experimental measurement in the range 0–10%. However, for 25% doping concentration, the bandgap increases matches well with the experimental behavior. To explain this behavior, the partial density of states should be analyzed (see Figs. 7b and 8b). In the case of undoped ZnO, the conduction band was produced by the 4s–Zn states, while the valence band was formed by the 2p–O states, respectively. When the doping process was applied, the conduction band was created by the hybridization between 3p–Al and 4s–Zn. It is clear from the band structure that the presence of Al leads to a shift in the conduction band to lower energy region, causing a decrease in the bandgap [49, 50]. The origin of this decrease is due to an increase in the bond length between Zn and O. On the similar lines, the increase in the bandgap upon doping with 25% of Al can be explained.

4 Conclusion

ZnO thin films doped with aluminum were successfully prepared by FCM-CVD technique. The films obtained were highly crystalline in nature, and no secondary phases were observed in the XRD results. The doping process affects the growth of the films, and the increase in the doping concentration was escorted by a change in the preferential orientation of the growth from (002) to (100).

In case of ZnO thin films doped with 5% and 10% Al concentration, the charge density increased and the optical bandgap decreased, indicating more absorption of the solar spectrum, and therefore, these films could serve as a satisfactory photocatalyst for the photocatalysis applications.

In case of high doping concentration (25% and 50%), the transmittance reached higher values along with an increase in the bandgaps. These samples are found to be adequately useful in the transparent solar cells for photovoltaic applications. DFT calculations validated the experimental behavior and indicated that the Al atoms are soluble in the ZnO material. The direct dependence between the bandgap and the bond length was shown.

Acknowledgements The Authors would like to acknowledge the support through the R&D Initiative—Call for projects around phosphates APPHOS—sponsored by OCP (OCP Foundation, R&D OCP, Mohammed VI Polytechnic University, National Center of Scientific and technical Research CNRST, Ministry of Higher Education, Scientific Research and Professional Training of Morocco MESRSFC) under the project entitled *Development of a phosphate-based photocatalytic reactor prototype for the treatment and recycling of wastewater*, project ID: TRT-NAJ-01/2017.

References

1. R.K. Sonker, S. Sikarwar, S.R.R. Sabhajeet, B.C. Yadav, *Opt. Mater.* **83**, 342 (2018)
2. S. Hamrouni, M.S. AlKhalifah, M.S. El-Bana, S.K. Zobaidi, S. Belgacem, *Appl. Phys. A* **124**, 555 (2018)
3. N. Bano, I. Hussain, O. Nur, M. Willander, H.S. Kwack, D.S. Dang, *Appl. Phys. A* **100**, 467 (2010)
4. N. Kaymak, E. Efil, E. Seven, A. Tataroğlu, S. Bilge, E.Ö. Orhan, *Mater. Res. Express* **6**, 026309 (2018)
5. Q. Yang, K. Tang, J. Zuo, Y. Qian, *Appl. Phys. A* **79**, 1847 (2004)
6. C. Wang, H. Fan, X. Ren, J. Fang, *Appl. Phys. A* **124**, 99 (2018)
7. P.-T. Hsieh, Y.-C. Chen, K.-S. Kao, C.-M. Wang, *Appl. Phys. A* **90**, 317 (2007)
8. J. Nishio, M. Tokumura, H.T. Znad, Y. Kawase, *J. Hazard. Mater.* **138**, 106 (2006)
9. Q.H. Li, D. Zhu, W. Liu, Y. Liu, X.C. Ma, *Appl. Surf. Sci.* **254**, 2922 (2008)
10. A. Raidou, F. Benmalek, T. Sall, M. Aggour, A. Qachaou, L. Laanab, M. Fahoume, *OALib* **01**, 1 (2014)
11. C. Zhu, T. Zhou, F. Shi, W. Song, J. Li, W. Wu, *Appl. Phys. A* **124**, 850 (2018)
12. A. Jamil, S. Fareed, N. Tiwari, C. Li, B. Cheng, X. Xu, M.A. Rafiq, *Appl. Phys. A* **125**, 238 (2019)
13. K. Nouneh, T. Ajjammouri, Z. Laghfour, A. Maaroufi, M. Abd-Lefdil, D. Chaumont, Z. Sekkat, *Mater. Lett.* **139**, 26 (2015)
14. W. Lu, D. Zhu, *Appl. Phys. A* **125**, 68 (2019)
15. M. Fahoume, O. Maghfoul, M. Aggour, B. Hartiti, F. Chraïbi, A. Ennaoui, *Sol. Energy Mater. Sol. Cells* **90**, 1437 (2006)
16. U. Chaitra, M.G. Mahesha, D. Kekuda, K.M. Rao, *Appl. Phys. A* **125**, 394 (2019)
17. K. Ghosh, R.K. Pandey, *Appl. Phys. A* **125**, 98 (2019)
18. S. Goudarzi, K. Khojier, *Appl. Phys. A* **124**, 601 (2018)
19. V. Kumar, H. Sharma, S.K. Singh, S. Kumar, A. Vij, *Appl. Phys. A* **125**, 212 (2019)
20. T. Kawaharamura, H. Nishinaka, S. Fujita, *Jpn. J. Appl. Phys.* **47**, 4669 (2008)
21. K. Ozga, T. Kawaharamura, A.A. Umar, M. Oyama, K. Nouneh, A. Slezak, S. Fujita, M. Piasecki, A.H. Reshak, I.V. Kityk, *Nanotechnology* **19**, 185709 (2008)
22. H.-J. Jeon, S.-G. Lee, K.-S. Shin, S.-W. Kim, J.-S. Park, *J. Alloys Compd.* **614**, 244 (2014)
23. T. Kawaharamura, H. Nishinaka, Y. Kamaka, Y. Masuda, J.-G. Lu, S. Fujita, *J. Korean Phys. Soc.* **53**, 2976 (2008)
24. R.J. Lang, *J. Acoust. Soc. Am.* **34**, 6 (1962)
25. P. Giannozzi, S. Baroni, N. Bonini, M. Calandra, R. Car, C. Cavazzoni, D. Ceresoli, G.L. Chiarotti, M. Cococcioni, I. Dabo, A. Dal Corso, S. de Gironcoli, S. Fabris, G. Fratesi, R. Gebauer, U. Gerstmann, C. Gougoussis, A. Kokalj, M. Lazzeri, L. Martin-Samos, N. Marzari, F. Mauri, R. Mazzarello, S. Paolini, A. Pasquarello, L. Paulatto, C. Sbraccia, S. Scandolo, G. Sclauzero, A.P. Seitonen, A. Smogunov, P. Umari, R.M. Wentzcovitch, *J. Phys. Condens. Matter.* **21**, 395502 (2009)
26. J.P. Perdew, K. Burke, M. Ernzerhof, *Phys. Rev. Lett.* **77**, 3865 (1996)
27. H.J. Monkhorst, J.D. Pack, *Phys. Rev. B* **13**, 5188 (1976)
28. S. Haller, J. Rousset, G. Renou, D. Lincot, *EPJ Photovolt.* **2**, 20401 (2011)
29. J.-L. Zhao, X.-M. Li, J.-M. Bian, W.-D. Yu, C.-Y. Zhang, *J. Cryst. Growth* **280**, 495 (2005)
30. M. Bizarro, *Appl. Catal. B Environ.* **97**, 198 (2010)
31. M. Bizarro, A. Sánchez-Arzate, I. Garduño-Wilches, J.C. Alonso, A. Ortiz, *Catal. Today* **166**, 129 (2011)
32. C.-H. Zhai, R.-J. Zhang, X. Chen, Y.-X. Zheng, S.-Y. Wang, J. Liu, N. Dai, L.-Y. Chen, *Nanoscale Res. Lett.* **11**, 407 (2016)
33. B.D. Cullity, J.W. Weymouth, *Am. J. Phys.* **25**, 394 (1957)
34. O. Daoudi, Y. Qachaou, A. Raidou, K. Nouneh, M. Lharch, M. Fahoume, *Superlatt. Microstruct.* **127**, 93 (2018)
35. M.K. Puchert, P.Y. Timbrell, R.N. Lamb, *J. Vac. Sci. Technol. Vac. Surf. Films* **14**, 2220 (1996)
36. G.A. Kumar, M.V.R. Reddy, K.N. Reddy, *IOP Conf. Ser. Mater. Sci. Eng.* **73**, 012133 (2015)
37. J. Mathew, J. Mathew, S.O.P. Trans, *Nano-Technol.* **1**, 1 (2014)
38. T.P. Rao, M.S. Kumar, V. Ganesan, *Indian J. Phys.* **85**, 1381 (2011)
39. B.K. Sharma, N. Khare, *J. Phys. Appl. Phys.* **43**, 465402 (2010)
40. J. Mass, P. Bhattacharya, R.S. Katiyar, *Mater. Sci. Eng. B* **103**, 9 (2003)
41. S. Shanthi, C. Subramanian, P. Ramasamy, *Mater. Sci. Eng. B* **57**, 127 (1999)
42. J. Tauc, A. Menth, *J. Non-Cryst. Solids* **8**, 569 (1972)
43. K. Dakhsi, B. Hartiti, S. Elfarrass, H. Tchognia, M.E. Touhami, P. Thevenin, *Mol. Cryst. Liq. Cryst.* **627**, 133 (2016)
44. M.H. Yoon, S.H. Lee, H.L. Park, H.K. Kim, M.S. Jang, *J. Mater. Sci. Lett.* **21**, 1703 (2002)
45. S. Yoshioka, F. Oba, R. Huang, I. Tanaka, T. Mizoguchi, T. Yamamoto, *J. Appl. Phys.* **103**, 014309 (2008)
46. P. Banerjee, W.-J. Lee, K.-R. Bae, S.B. Lee, G.W. Rubloff, *J. Appl. Phys.* **108**, 043504 (2010)
47. J.-Q. Wen, J.-M. Zhang, Z.-Q. Li, *Opt. Int. J. Light Electron. Opt.* **156**, 297 (2018)
48. S.H. Deng, M.Y. Duan, M. Xu, L. He, *Phys. B Condens. Matter.* **406**, 2314 (2011)
49. H. Ahmoum, M. Boughrara, M.S. Su'ait, M. Kerouad, *Chem. Phys. Lett.* **719**, 45 (2019)
50. H. Ahmoum, M. Boughrara, M.S. Su'ait, S. Chopra, M. Kerouad, *Phys. B Condens. Matter.* **560**, 28 (2019)

Publisher's Note Springer Nature remains neutral with regard to jurisdictional claims in published maps and institutional affiliations.